Nanoscale

PAPER

View Article Online
View Journal | View Issue

Cite this: *Nanoscale*, 2022, **14**, 18143

Growth suppression of bacteria by biofilm deterioration using silver nanoparticles with magnetic doping†

Rafael Torres-Mendieta, *[a] Nhung H. A. Nguyen, [a] Andrea Guadagnini,[b] Jaroslav Semerad,[c] Dariusz Łukowiec,[d] Petr Parma,[a,e] Jijin Yang,[b] Stefano Agnoli, [b] Alena Sevcu, [a] Tomas Cajthaml, [c] Miroslav Cernik[a] and Vincenzo Amendola *[b]

Decades of antibiotic use and misuse have generated selective pressure toward the rise of antibiotic-resistant bacteria, which now contaminate our environment and pose a major threat to humanity. According to the evolutionary "Red queen theory", developing new antimicrobial technologies is both urgent and mandatory. While new antibiotics and antibacterial technologies have been developed, most fail to penetrate the biofilm that protects bacteria against external antimicrobial attacks. Hence, new antimicrobial formulations should combine toxicity for bacteria, biofilm permeation ability, biofilm deterioration capability, and tolerability by the organism without renouncing compatibility with a sustainable, low-cost, and scalable production route as well as an acceptable ecological impact after the ineluctable release of the antibacterial compound in the environment. Here, we report on the use of silver nanoparticles (NPs) doped with magnetic elements (Co and Fe) that allow standard silver antibacterial agents to perforate bacterial biofilms through magnetophoretic migration upon the application of an external magnetic field. The method has been proved to be effective in opening micrometric channels and reducing the thicknesses of models of biofilms containing bacteria such as *Enterococcus faecalis*, *Enterobacter cloacae*, and *Bacillus subtilis*. Besides, the NPs increase the membrane lipid peroxidation biomarkers through the formation of reactive oxygen species in *E. faecalis*, *E. cloacae*, *B. subtilis*, and *Pseudomonas putida* colonies. The NPs are produced using a one-step, scalable, and environmentally low-cost procedure based on laser ablation in a liquid, allowing easy transfer to real-world applications. The antibacterial effectiveness of these magnetic silver NPs may be further optimized by engineering the external magnetic fields and surface conjugation with specific functionalities for biofilm disruption or bactericidal effectiveness.

Received 15th July 2022,
Accepted 21st November 2022

DOI: 10.1039/d2nr03902h

rsc.li/nanoscale

Introduction

Like any other living organism, bacteria are continuously adapting to their environment to ensure their continued existence.[1,2] However, in a highly competitive ecosystem, like that of an industrialized society where antibiotics and antimicrobial agents have been used and abused for over a century, bacteria have developed several new abilities that enable their survival and proliferation.[1] A key feature among these is the ability to adhere to different surfaces and segregate a matrix of extracellular polymeric substances (EPSs) which contaminates our living environment.[2] This EPS matrix protects bacteria from external threats, such as drugs, and enables them to proliferate in the form of biofilms.[3] These bacterial biofilms have been shown to coat equipment used for the delivery and management of water;[4,5] medical instruments and implants, resulting in hospital-acquired infections;[6] and the insides of plants and animals, including humans, provoking persistent infections.[7] As such, bacterial evolution has translated into a significant hazard to the human environment.

[a]*Institute for Nanomaterials, Advanced Technologies and Innovation, Technical University of Liberec, Studentská 1402/2, 461 17 Liberec, Czech Republic. E-mail: Rafael.Torres@tul.cz*
[b]*Department of Chemical Sciences, University of Padova, Padova, I-35131 Italy. E-mail: vincenzo.amendola@unipd.it*
[c]*Institute of Microbiology of the Czech Academy of Sciences, Vídeňská 1083, Prague 4, Czech Republic*
[d]*Materials Research Laboratory, Faculty of Mechanical Engineering, Silesian University of Technology, Konarskiego 18A St., 44-100 Gliwice, Poland*
[e]*Faculty of Mechanical Engineering, Technical University of Liberec, Studentska 2, 461 17 Liberec, Czech Republic*

† Electronic supplementary information (ESI) available. See DOI: https://doi.org/10.1039/d2nr03902h

The evolutive "Red Queen" theory[8] clearly states that humanity has only one means of fighting this threat in order to survive, *i.e.*, the development of new and more powerful antimicrobial technologies. Over the last century, several different technologies have been developed, depending on the nature of the bacteria, including mechanical or chemical removal of biofilms from accessible locations or antibiotic treatments for those lodged inside living organisms. However, to date, the evolutionary mechanisms of biofilm formation have guaranteed bacterial survival under both eradication treatments. On the one hand, during mechanical removal, any remaining 'debris' located in difficult-to-access sites may serve as a nutrient reservoir and/or seed for scaffold formation, facilitating bacterial regrowth.[2] On the other hand, when using antibiotic chemical therapies, the biofilm acts as a shield, ensuring that only those bacteria at the biofilm's surface suffer damage while those inside remain unaffected.[9] This induced bacteria to develop resistance against current antibiotics, leading to the frightening prediction that bacteria-related diseases could well become one of the principal causes of death in the near future.[1] Thus, even when potent broad-spectrum drugs against pathogenic bacteria are developed, their efficiency relies on the drug's ability to overcome the protective biofilm barrier, which indirectly determines how long it will take to develop a new generation of resistant microorganisms.[2] The environmental impact of antibacterial technologies is worsened by bacterial resistance, which implies higher doses and dispersion of antibiotic substances in the environment, as well as the resorting to synthetic procedures with a lower level of sustainability and cost.[10,11]

One of the newest and most promising approaches for tackling the challenge of the growth suppression of infectious bacteria relies on the development of magnetic nanoparticles (NPs) carrying bactericidal elements.[12] Magnetic NPs respond to external magnetic fields, allowing mechanical damage to the biofilm through particle penetration, mechanical disruption, and the creation of highways for the permeation of antibacterial drugs.[13] Other potential benefits of this process are that magnetic field generation is inexpensive, it can penetrate a wide variety of materials over relatively long distances, it is insensitive to the surface morphology (*e.g.*, tight or deep locations), and it is not harmful to humans or destructive to objects.[14]

The most frequently used ferromagnetic elements for the generation of magnetically motile motors are cobalt (Co)[15,16] and iron (Fe).[17,18] In addition to their magnetic responsiveness, these elements are intensively employed in bacterial treatment due to their capacity to generate reactive oxygen species (ROS) through Fenton reactions with H_2O_2, which is produced by different microorganism metabolic processes.[19,20] This has resulted in their use to degrade EPS matrices and eradicate biofilms with the help of either H_2O_2 [21] or antimicrobial drugs such as gentamicin.[13] However, alternative approaches have also been explored recently, including doping the surface of magnetic NPs with more potent antibacterial agents such as antibiotics[22] or silver (Ag) NPs,[17] the latter being considered the most prominent antibacterial nanoelement.[14,23] Unlike standard antibiotic compounds, which generally bind to bacterium-specific receptors, the Ag NP antibacterial mechanism relies on its ability to produce ROS and subsequently penetrate the bacterial membrane. This dramatically reduces the bacteria's chances of developing resistance and greatly increases their bactericidal action spectrum.[24] However, this scenario is only possible when the Ag NPs, or their released Ag^+ ions, can penetrate through the protective biofilm layer.[14,25] To this end, research efforts have been directed toward developing dual-function magnetic-antibacterial Ag NPs and their successful deployment as recyclable disinfection agents. Magnetic Ag NPs (MSNPs) have the ability to arrest the growth of antibiotic-resistant bacteria, thus preventing biofilm formation,[26] or can be employed as dual-functional platforms for detecting and inhibiting bacteria.[27] Moreover, the synergy between Ag and magnetic elements such as Fe may enhance its antimicrobial behavior,[28] leading to more powerful antimicrobial action against multi-drug resistant pathogens.[29]

Most MSNPs are obtained as heterostructures or core–shells through sequential synthetic steps, which are energy-consuming and have a heavy environmental footprint due to chemical by-product generation. This is an issue, considering that Ag NPs are produced on the tons scale annually.[30,31] On the other hand, the ecological impact of Ag NPs has been the object of serious concern in recent years. Bacteria showed the ability to develop resistance against Ag NPs after prolonged exposure, in analogy to what happened after decades of misuse of molecular antibiotics.[30,32,33] Besides, the release of Ag NPs in the environment, which is ineluctable due to their widespread exploitation in various products, may also compromise the diversity and abundance of microbes in natural ecosystems, including those involved in the nitrogen cycle and decomposition of organic matter.[31] These studies point to a more careful use of Ag NPs and a careful evaluation of the risk/benefits ratio, including after NP disposal,[30,31] which are soothed by the availability of more effective antimicrobial formulations exploitable at lower doses.

Here, we report on the production of Ag NPs doped with the magnetic elements Co and Fe and describe their exploitation for growth suppression of potentially pathogenic and non-pathogenic bacteria through biofilm deterioration. In doing so, we describe how readily the MSNPs respond to an external magnetic field, which would enhance mechanical interactions with bacterial biofilms, facilitating the antibacterial activity of Ag NPs added to the system by increasing the rate of oxidative stress. The MSNPs are produced in a single step using Laser Ablation in Liquid (LAL),[34] a low-cost and environmentally friendly method with a self-standing automatic setup.[34] This is one of the leading techniques for the preparation of multi-element metal NPs,[34–37] especially when element immiscibility prevents the use of standard synthetic routes such as the wet-chemistry approach, which runs under thermodynamic equilibrium. A key feature of LAL is that the NPs are obtained free of stabilizing agents or organic contaminants,[34] meaning that they can be tested pure or after surface conjugation with

specific ligands,[38] such as suitably designed antibacterial or biofilm penetrating agents.

Materials and methods

Synthesis

Ag, AgCo, and AgFe NPs were produced using a slight modification of the LAL protocol described in previous studies.[35,36,39] In brief, pulses of an Nd-YAG laser (1064 nm, 6 ns, 50 Hz) were focused with an f 100 mm lens onto a metal target (99.99% pure Ag from Sigma-Aldrich, 99.9% pure Ag : Co 1 : 1 and Ag : Fe 1 : 1 foils from Mateck GmbH) immersed in ethanol (HPLC grade, Sigma-Aldrich) with 0.2% vol/vol of distilled water. All targets were stored in a moisture-free environment using a vacuum sealer and rinsed only with ethanol to ensure the target surface remained unmodified over time. Target polishing before synthesis was avoided because of the progressive changes in reflectivity and surface properties during the LAL procedure, with possible changes in NP structure and composition during each laser synthesis.[34,40] Laser fluence was set to 20 J cm^{-2} and the ablated target area was set to 7 mm × 2 mm in 300 s by mounting the ablation cell on a motorized XY scanning stage (Standa) managed with a 2-axis stepper and a DC motorized controller. Following LAL, the colloidal solution was diluted in a 1 : 1 ratio with an aqueous solution containing ethylenediaminetetraacetic acid disodium salt dihydrate (disodium EDTA, Sigma-Aldrich, 3 mg mL^{-1}) and kept at 30 °C for 1 h, after which the nanoparticles were washed three times with distilled water by centrifugation at 3000 rcf and redispersed in distilled water.

Characterization

Dynamic light scattering (DLS) and z-potential measurements were performed with a Zetasizer Nano ZS90 (Malvern Instruments Ltd) with a laser wavelength centered at 632.8 nm, and the detector placed at a scattering angle of 173°. The UV-visible spectra were recorded with a JASCO V770 spectrometer using 2 mm optical path quartz cells. A NexION 3000D Inductively Coupled Plasma Mass Spectroscope (ICP-MS; PerkinElmer; detection limit 0.5 ppt) was employed to ascertain the atomic composition of the NPs. The release of Ag, Co, and Fe ions from the NPs was examined using the same instrument operated in the single-particle mode (spICP-MS). For this, the transient data acquisition speed was set at <100 μs in order to observe the ion clouds from individual particles[41,42] and the baseline was taken after calibration of the instrument by employing the corresponding standard. The samples were diluted in a physiological solution (PS; 0.9% NaCl) to 50 ng L^{-1} (0.05 ppb) to avoid misinterpretation due to the overlapping of signals from different particles.[41] Each sample was later measured at 12 different time points (0, 1, 2.5, 4.5, 25, 48, 72, 96, 120, 144, 168, and 504 h). Moreover, given the difficulty of measuring Fe using spICP-MS at such low concentrations, it was necessary to do it in the gas mode (ammonia flow rate of 0.3 mL min^{-1}).[43] The NP morphology and elemental composition were assessed using a TITAN 80-300 (FEI) Scanning Transmission Electron Microscope (STEM) operating at 300 kV. In addition, the EDX spectra were recorded using an X-Max 80 detector (Oxford Instruments). X-ray photoelectron spectroscopy (XPS) analysis was performed with a modified VG ESCALAB MKII (Vacuum Generators, UK) equipped with Mg and Al X-ray sources, a sputter gun, and a hemispherical electrostatic analyzer with a five-channel detector. The samples were obtained by dropwise deposition of the NP dispersion onto a copper (Cu) sample holder and drying at room temperature. X-ray diffraction (XRD) analysis with a Panalytical XPert 3 powder diffractometer equipped with a Cu tube (40 kV, 40 mA), a BBHD mirror, a spinner, and a PlXcel detector was performed on NPs deposited on Si zero-background substrates by drop-casting and drying at room temperature. Crystalline phase identification and Rietveld analysis were performed using the Panalytical High Score Plus 4 software and Panalytical ICSD, PDF2, and COD databases.

Bacterial culture and exposure conditions

Gram-negative *E. cloacae* CCM 1903 and *P. putida* CCM 7156 and Gram-positive *E. faecalis* CCM 4224 and *B. subtilis* CCM 1999 bacteria were obtained from the Czech Collection of Microorganisms, Masaryk University, Brno, Czech Republic (**https://www.sci.muni.cz/ccm/**). Bacterial inocula were always prepared fresh from 1–2 colonies growing overnight in a soya nutrient broth (Sigma-Aldrich, USA) at 37 °C (*E. cloacae* and *E. faecalis*) or 30 °C (*P. putida* and *B. subtilis*) while shaking at 200 rpm. The overnight cultures were centrifuged to obtain pellets, which were then resuspended and diluted using a physiological solution (PS; 0.9% NaCl) to achieve an optical density (OD) of 0.6 at 600 nm using a DR6000 UV-visible spectrophotometer (Hach Lange). To determine the Minimal Effective Concentration (MEC), the bacteria were exposed to different nanocolloids (Ag NPs, AgCo NPs, and AgFe NPs dispersed in PS), and afterward, a spot test was performed by modifying the procedure initially described by Suppi *et al.*[44] Briefly, 100 μl of the suspended bacteria was pipetted into each well of a 96 well-plate, after which 100 μl of various concentrations of the nanocolloids were added to each well by two-fold dilution: 100, 50, 25, 12.5, 5.25, 3.125, and 1.5625 μg ml^{-1}. Each 96-well plate was incubated under the same growth conditions: *E. cloacae* and *E. faecalis* at 37 °C and *P. putida* and *B. subtilis* at 30 °C. The bacteria were exposed to the NPs for 3 h (short-term exposure) and 24 h (medium-term exposure), after which 5 μl from each well plate was pipetted onto a Petri dish containing an agar growth medium and incubated for 24 h. Finally, bacterial growth was observed on each spot, with the lowest NP concentration (labeled as "+") able to inhibit cells from forming visible colonies and defined as MEC. The wells with bacteria cells without NPs were considered as the control.

Biofilm preparation

Resuspended cultures of all bacteria were prepared as described above, after which they were transferred to a 24 well-

plate (1 mL to each well). The plates were kept at room temperature for 2 h, allowing bacterial cell adhesion, after which the PS was removed and washed twice with sterilized PS before adding the fresh soya nutrient medium. Finally, the plates were incubated for 16 h under bacterial growth conditions to obtain bacterial biofilms.

Biofilm perforation experiments

After 16 h, the soya nutrient growth medium was removed, and the biofilm was washed twice with sterilized PS. The NPs (Ag, AgCo, and AgFe NPs) were added into the wells in two concentrations, the MEC for each bacterial type and a high concentration (HC) of 20 μm mL^{-1}. A square nickel-plated NdFeB magnet (80 × 80 × 20 mm, N45) was first placed under the plates for 1.5 min and subsequently circled around the well for a further 1.5 min to force NP movement through the biofilm. This magnetically forced NP movement was repeated three times using the same cycle (9 min in total). After completing the three cycles, the biofilms were prepared for observation by confocal microscopy.

Confocal microscopy

Biofilm observation was performed using an Olympus FV1000 TIRF Confocal Laser Scanning Microscope (CLSM; Olympus) with a LUCPLFLN 20× NA: 0.45 objective lens. Prior to microscopic examination, the exposed biofilms in the 24-well plates were washed twice with phosphate-buffered saline (PBS) and then stained with 1 mL of diluted SYBR green solution for 15 min at room temperature under darkness. The SYBR green stain was excited by the microscope's argon laser at 473 nm, and the corresponding fluorescence was measured at 520 nm. Transverse cross-sectional images were collected under the XZ confocal scanning mode, with a section thickness of 1 μm. Multiple images were used to analyze biofilm damage inflicted by the particles (channel formation and relative biofilm thickness).

MDA assay

Determination of malondialdehyde (MDA) in biofilms exposed to different NP types was performed according to a recently published method,[45] with slight modifications in the extraction protocol to optimize the assay for bacterial biofilm exposure. Briefly, MDA was extracted from the bacterial biofilm culture with 1 mL of 10% trichloroacetic acid (10 min under darkness) and centrifuged at 10 000 rcf for 15 min to remove the NPs and cellular debris. Finally, the extracted MDA was derivatized with thiobarbituric acid and analyzed using High-Performance Liquid Chromatography with Fluorescence Detection (HPLC-FLD).[45] MDA production is expressed as the mean of three independent replicates with their respective standard deviations.

Cell cytotoxicity

The cytotoxicity of Ag, AgFe and AgCo NPs was assessed in human cells (T47D—breast carcinoma) and rainbow trout cells (RT—gills) using previously published protocols.[46,47] Briefly, both cell lines were exposed for 24 h to various NP concentrations (1, 5, 10, 20, 40, and 60 mg L^{-1}). The concentrations were selected considering the HC used in the biofilm deterioration experiments as the middle value. The NPs were dispersed in the minimal essential medium L15ex. After the incubation time, the cells were rinsed and incubated again at room temperature for 30 min in 100 μl of either 1.25% of AlamarBlue (AB) or 4 μM of 5-carboxyfluorescein diacetate-acetoxymethyl ester (CFDA-AM) in L15ex. The AB dye was used to assess the cellular metabolic activity and CFDA-AM to determine the cell membrane integrity. After the incubation in both dyes, the cell fluorescence was measured using an Infinite M200 PRO microplate reader (Tecan). The excitation wavelength was 532 and 485 nm for AB and CFDA-AM, respectively, and the emission wavelength was 590 and 535 nm.

Results and discussion

NP structures

A key point for any antibacterial agent is the ability to produce the agent in scalable amounts, at low cost, and in a sustainable manner, particularly in light of the current global efforts toward a circular economy. The most straightforward approach for generating NPs containing Ag, Fe, or Co is through the production of nanoalloys. Unfortunately, the Hume–Rothery rules[48] state that miscibility is not possible when (i) the atomic radii of the solute and solvent atoms differ by more than 15% (Ag = 160 pm, Co = 135 pm, and Fe = 140 pm), (ii) the crystal structures of the solute and solvent differ (Ag = face-centered cubic, Co = hexagonal close-packed, and Fe = body-centered cubic), (iii) the solvent and solute have differing valency (Ag = 1 and Co and Fe = 2 in their metallic state) or electronegativity (Ag = 1.93, Co = 1.88, and Fe = 1.83). In fact, the thermodynamic phase diagrams of Ag and Co or Fe show total immiscibility, even at a few at% of one element in the other.[49,50] In addition, Co and Fe readily undergo oxidation in air,[51,52] contributing to element segregation.[53] To this end, LAL has been applied because it is an out-of-equilibrium synthetic approach that allows immiscible elements to be frozen together at the nanoscale.[35,36,39,54] The Co-doped or Fe-doped Ag NPs were obtained *via* laser ablation of bimetallic AgCo or AgFe targets dipped in ethanol with 0.2% vol/vol distilled water. This is a slight modification to previously published procedures for bimetallic AgCo and AgFe NPs[35,36,39] that allows for boosting productivity by adding minimal amounts of distilled water.[55] The resulting doped NPs were then transferred from the ethanol solution to an aqueous environment by centrifuging after treatment with ethylenediaminetetraacetic acid (EDTA) at 30 °C for 1 h to remove excess Fe or Co compounds unbound to Ag.

Once redispersed in water, the particles display bimodal hydrodynamic size distributions (Fig. 1A) that are equivalent to those of pure Ag NPs obtained through the same procedure. The slight size decrement displayed by AgCo and AgFe NPs may be indicative of a more significant surface charge than

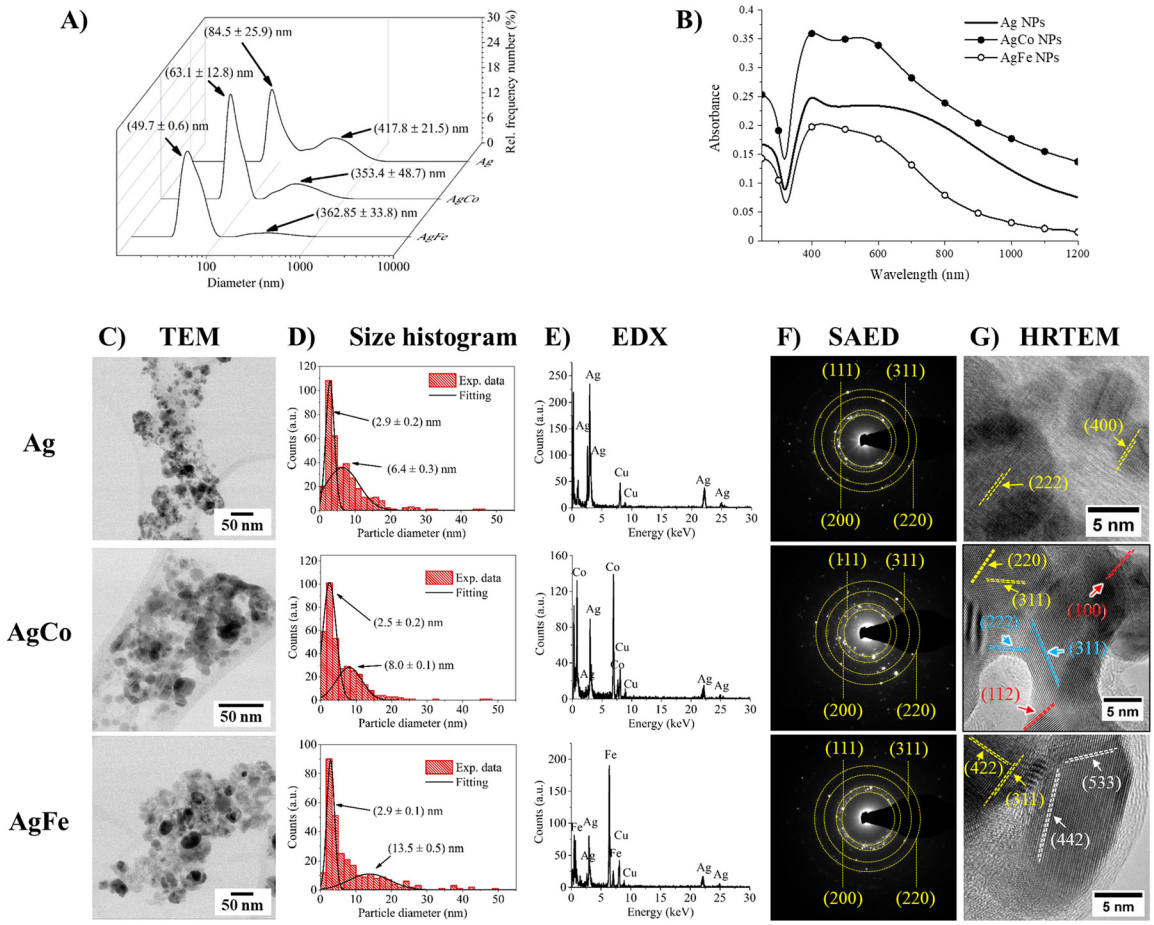

Fig. 1 (A) Hydrodynamic size distribution and (B) the optical absorption spectra of Ag, AgCo, and AgFe NPs dispersed in pure water. (C) Transmission electron microscopy (TEM) images of Ag, AgCo, and AgFe NPs, (D) size histograms, (E) energy-dispersive X-ray spectroscopy (EDX) patterns displaying the elements found in each sample, (F) selected area electron diffraction (SAED) patterns, where only Ag is visible, and (G) high-resolution transmission electron microscopy (HRTEM) images displaying the crystal families found in the samples. Note that in the HRTEM images, yellow corresponds to Ag, red to hexagonal CoO, blue to cubic CoO, and white to Fe_3O_4.

pure Ag NPs. As several studies[56] have shown that NP surface charge plays a role in the antibacterial activity of Ag NPs, z-potential measurements were performed on samples dispersed in a physiological solution (PS). The results demonstrate that all NPs have a negative surface charge, with Ag NPs at −32.9 ± 2.8 mV, AgCo NPs at −41.5 ± 0.3 mV, and AgFe NPs at −38.6 ± 0.5 mV, which also implies colloidal stability.

The colloids' optical absorption spectra (Fig. 1B) clearly show the absorption band due to the surface plasmon resonance of pure or doped Ag NPs in all three samples, a feature also reported in previous studies related to the preparation of these MSNPs.[35,36,39] The presence of Fe and Co in the MSNPs was confirmed by ICP-MS, with the reference Ag NPs showing the presence of Ag only, CoAg NPs comprising 90 ± 9 at% Ag and 10 ± 1 at% Co, and FeAg NPs comprising 59 ± 6 at% Ag and 41 ± 4 at% Fe.

The MSNP structure was assessed *via* transmission electron microscopy (TEM) micrographs, which confirmed that NPs in the agglomerates have a bimodal size distribution (Fig. 1C and D). As recently demonstrated using molecular dynamics calculations,[57] bimodality is typical of LAL due to the production of large particles through hydrodynamic instability at the interface between the heated target and the above-lying vaporized solvent layer, while smaller particles are produced by vaporization in the metal-liquid mixing region.[57] The resulting small-sized NPs have comparable average diameters of 2.9 ± 0.2 nm, 2.5 ± 0.2 nm, and 2.9 ± 0.1 nm for Ag, AgCo, and AgFe NPs, respectively. Instead, the average sizes of the larger particles are 6.4 ± 0.3 nm, 8.0 ± 0.1 nm, and 13.5 ± 0.5 nm for Ag, AgCo, and AgFe NPs, respectively. Since the hydrodynamic size assessed by DLS is larger, the NPs formed nanometric aggregates during the centrifugation step of the cleaning procedure. This happens because we are employing ligand-free NPs. Although NP aggregation is associated with the decrease in the active area for Ag ion release,[58] the absence of stabilizing ligands is essential for maintaining the NP surface free and facilitating the effective release of Ag^+ ions despite aggregation.[23] Besides, the size of the NPs measured by TEM is only a few nm, which warrants a high specific surface per unit mass in the aggregates.

Based on their Selected Area Electron Diffraction (SAED) patterns, an Ag face-centered cubic crystalline structure with an *Fm*$\bar{3}$*m* phase (International Centre for Diffraction Data; ICDD file: 65-2871) is clearly identified in all samples. This result was also confirmed by ensemble powder XRD analysis of dried NP samples (Fig. S1 in the ESI†). Furthermore, energy dispersive X-ray (EDX) analysis unequivocally identified Co and Fe peaks in AgCo and AgFe MSNPs (Fig. 1E), neither of which were detected in the reference Ag NPs. These results agree with all previous reports on these MSNPs, suggesting that Co and Fe are embedded as defects in the crystalline Ag scaffold, clearly seen during the electron diffraction analysis of all three samples (Fig. 1F). However, the same studies also highlighted ineluctable surface oxidation of Co and Fe in these NPs, which, in our case, may be favored by the 0.2% water in the ethanol used during LAL. High-Resolution TEM (HRTEM; Fig. 1G) also shows the presence of crystalline domains with interplanar spacing ascribable to Co or Fe oxides (CoO, Fe_3O_4). These regions are either found around Ag crystals or forming necks between them. Due to the ultrasmall crystalline size, corresponding to broad diffraction peaks, and the lower X-ray scattering cross section compared to Ag, the Co and Fe oxide phases were not found in the XRD patterns of AgFe and AgCo NPs, in accordance with what is reported in previous studies on similar bimetallic NPs.[36,39]

In more detail, in the AgCo MSNPs, it is possible to find zones connecting Ag NPs where the *d*-spacings match either the cubic CoO crystal with the space group *Fm*3*m* (ICDD: file 43-1004) or the hexagonal CoO crystal with the space group *P*63*mc* (ICDD file: 89-2803). In the case of AgFe MSNPs, the connection zones between the Ag domains are either associated with the cubic Fe_3O_4 space group *Fd*3*m* (ICDD file: 65-3107) or with the monoclinic ε-Fe_2O_3 space group *P* (ICDD file: 16-653).

To further substantiate the results of the TEM analysis, XPS was performed on the three samples. The photoemission line of the Ag $3d_{5/2}$ peak (Fig. 2A) is centered at a binding energy of 368 eV, typical of metallic Ag in all samples. In addition, the Auger parameter and the shape of the MNN Auger peak are located within the typical range of metallic Ag in all samples (Fig. 2B).[59] The Co 2p peaks comprise several components with a complex multiplet structure, with the Co $2p_{3/2}$ and Co Auger peaks overlapping, while the Co $2p_{1/2}$ peak fits well with Co(II) oxide (802–793 eV) and a minority of metallic Co (792 eV) (Fig. 2C). The Fe 2p peaks also have a complex multiple-component structure, with the Fe $2p_{1/2}$ and Ag 3s peaks overlapping, while the Fe $2p_{3/2}$ peak fits well with Fe(III) and Fe(II) multiplets appropriate for magnetite (Fe_3O_4, 715–707 eV) and a fraction of metallic Fe (706.5 eV) (Fig. 2D). In previous XPS analyses for Ag NPs doped with Co or Fe,[35,36,39] the metal component is found inside the particles, while transition metals with a higher oxidation state dominate on the surface, as expected in an aqueous environment. Surface stoichiometry extracted from the XPS analyses indicates ratios of 77 : 23 for Ag : Co and 60 : 40 for Ag : Fe. The AgFe NP value agrees with the bulk value obtained from ICP-MS analysis, while the AgCo NP value suggests segregation of Co at the surface.

Previous studies indicated that a comparable percentage of Fe and Co was found in AgFe and AgCo NPs synthesized by LAL in pure ethanol (20 at% for AgFe and 17 at% for AgCo).[36,39] Due to the immiscibility of Fe or Co with Ag, this fraction resulted independently from the abundance of the transition element in the bulk target.[36,39] In the LAL synthesis in ethanol with 0.2% vol/vol of distilled water, the results indicate that the transition metals reacted with water molecules and formed oxidized compounds at the Ag NP surface, in addition to oxidized by-products that are eliminated by the cleaning protocol with EDTA. However, nanocrystalline cobalt oxides are more easily dissolved by EDTA than iron oxides.[60,61] This suggests that the lower cobalt fraction in AgCo NPs compared to the iron fraction in AgFe NPs is caused by the lower stability of cobalt oxide and the more effective dissolution during the NP cleaning procedure.

Ag^+ release

The dominant mechanism of Ag NP bacterial toxicity involves the release of Ag^+ ions through surface oxidation in a physiological environment, allowing the NPs to penetrate the cellular membrane and undergo ROS generation, ultimately leading to bacterial death.[62,63] While this mechanism has been shown to be independent of Ag NP size, it is crucially affected by surface chemistry and is hampered in Ag NPs capped with ligands or organic molecules.[64] In the case of MSNPs, a portion of the surface is occupied by oxidized Co or Fe atoms. Hence, the Ag^+ ion concentration was tracked over time using single-particle ICP-MS (spICP-MS) measurements. Co- and Fe-doped MSNPs

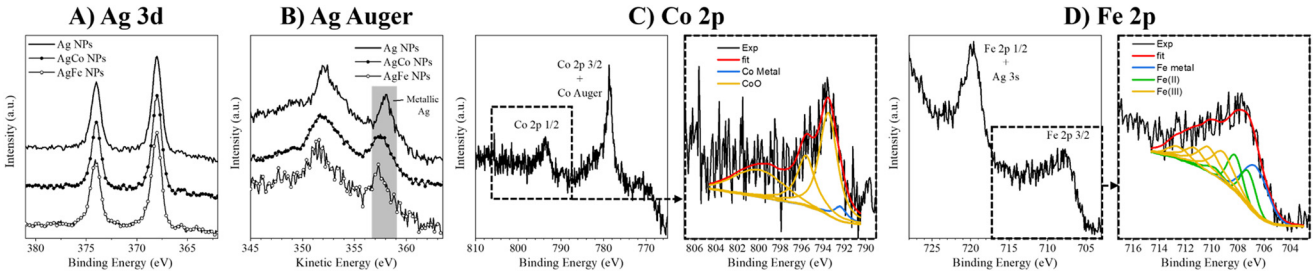

Fig. 2 XPS analyses of Ag, AgCo, and AgFe NPs. (A) Ag 3d peaks. (B) Ag Auger peaks, (C) Co 2p and Co Auger peaks and the fit of Co $2p_{1/2}$, (D) Fe 2p and Ag 3s and Fe $2p_{3/2}$ peaks.

and reference Ag NPs were diluted at 50 ng L^{-1} (0.05 ppb) in a physiological solution of 0.9% NaCl to reproduce the same pH and electrolyte content of the *in vitro* medium in which the bacteria are grown. The Ag- and AgFe NPs achieved maximum ion release at 25 h, after which ion release remained stable up to 504 h, *i.e.* 21 days, while the AgCo NPs reached maximum ion release at 72 h, thereafter remaining constant up to 504 h (Fig. 3A). However, both AgCo and AgFe NPs displayed lower Ag^+ release than pure Ag NPs after short- and medium-term exposures of 3 and 24 h, respectively.

The Ag^+ release rate is regulated by chemisorption and electron transfer of dissolved O_2 over the Ag NP surface;[64] however, as the AgCo and AgFe NPs in this study were synthesized without ligands, the presence of Fe or Co oxides at the particle surface is likely to reduce the number of possible Ag-chemisorption sites. This hypothesis was supported by the observation that lower Ag^+ release rates are recorded in AgFe NPs, which, according to both ICP-MS and XPS, also had the lowest atomic Ag abundance at the particle surface. On the other hand, the presence of Co in AgCo NPs appears to slow down Ag^+ release over short and medium-term exposures, though the release rate following long-time exposure (504 h) was the same as that for pure Ag NPs. It has been reported previously that Ag, Fe, and Co NPs experience ion release (Ag^+, Fe^{3+}, Fe^{2+}, and Co^{2+}, respectively) in a biological environment,[65–67] though ion release from Co oxides tends to be lower in physiological solutions.[68] Hence, the release of Fe and Co ions over time was also measured (Fig. S2 in ESI†). Even though the ion release of both elements was minimal compared to Ag, upon long-time exposure, Co was not detected anymore and Fe stayed constant. These data, thus, ratify that after the exhaustion of Co oxides at the surface of AgCo NPs, the number of Ag-chemisorption sites and Ag^+ release increased. Instead, the constant release of Fe ions agrees with the lower Ag^+ release of AgFe NPs compared to Ag and AgCo NPs upon long times of observation. In summary, the doping of Ag NPs with magnetic elements has an effect resembling the use of specific ligands, which provide a controlled release of Ag^+ ions over time compared to pure-Ag NPs.[23,62,65]

Antibacterial activity

In order to obtain a broad overview of the eradication behavior of MSNPs and the reference Ag NPs, MEC was determined for the opportunistic pathogenic bacteria *E. faecalis*[69] and *E. cloacae*[70] and the non-pathogenic *B. subtilis*[4] and *P. putida*[71] that are considered model bacteria capable of surviving in a range of environments and conditions, including hospitals, living organisms, and water management facilities.

The MEC value was defined as the lowest NP concentration, which inhibited cells from forming visible colonies (Fig. 3B and C). The values obtained for short (3 h) and medium (24 h) term exposure showed that pure Ag NPs had the lowest MEC value for all bacteria, with those for AgCo and AgFe NPs being consistently higher (Fig. 3D).

In the case of *E. faecalis* that is resistant to practically all antibiotics in use,[73] the rate of Ag^+ release from AgCo and AgFe NPs was too low to produce any antibacterial effect in the short-term, but both MSNPs were effective over the medium-term, with MEC values two orders of magnitude higher than that for Ag NPs alone. In the case of *E. cloacae*, which, being a Gram-negative bacteria, is less responsive to antibiotics, it was possible to observe a trend similar to that for *E. faecalis*. For

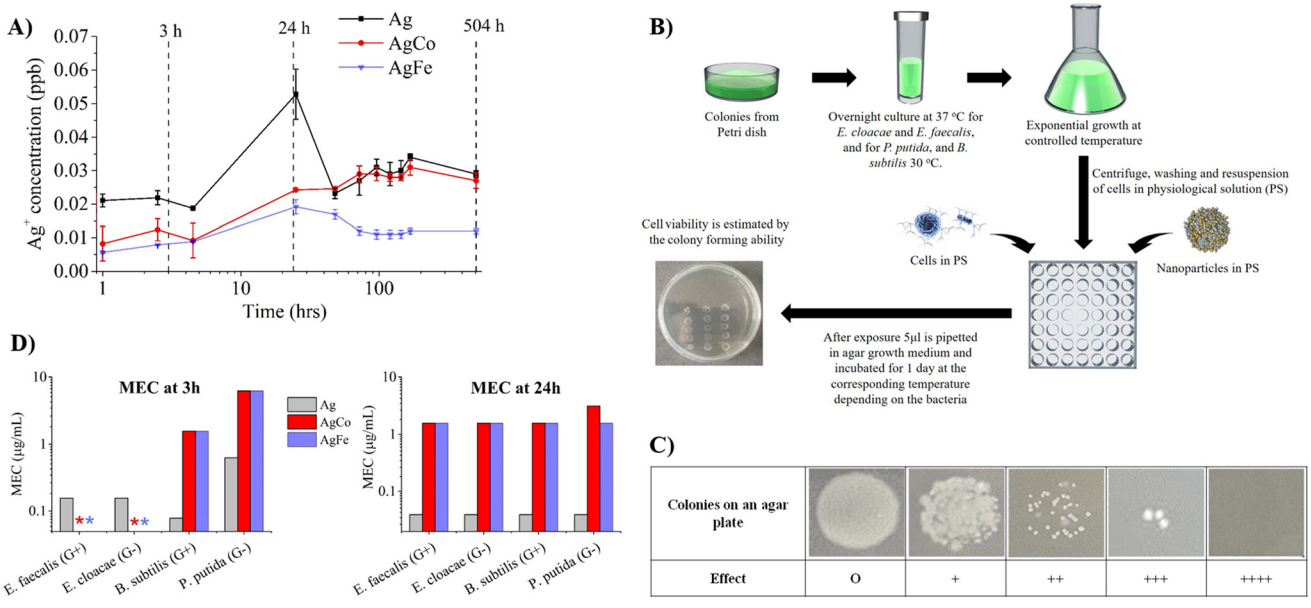

Fig. 3 (A) Release of Ag^+ ions at different times. (B) Scheme used for the "spot test". (C) Visual evidence of the bacterial growth after the spot test (for the spot test, "+" means bacterial growth inhibition, *i.e.*, the fewer visible colonies, the more the number of "+" symbols. In addition, "O" means lack of effect) and (D) the minimal effective concentration (MEC) expressed in µg mL^{-1} after 3 and 24 h (note the logarithmic scale). The no observed effect concentration (NOEC) of up to 100 µg mL^{-1} is represented with an asterisk. G+ = Gram-positive and G– = Gram-negative bacteria.

B. subtilis and *P. putida*, however, both MSNPs already displayed bactericidal behavior after short-term exposure, with a MEC one order of magnitude higher than that for Ag NPs at short-term exposure and two orders of magnitude higher after long-term exposure. Besides the evident benefit of eradicating pathogenic bacteria, non-pathogenic ones like *P. putida* are environmentally relevant for the development of superbugs because they may serve as exchange platforms for antibiotic resistance genes (ARG).[72]

Overall, the bactericidal behavior decreased in the order of Ag NPs > AgFe NPs > AgCo NPs (Fig. 3D), a pattern that agrees with the Ag^+ release rates measured by spICP-MS (Fig. 3A), suggesting that optimal effects may be obtained using mixtures of MSNPs and pure antibacterial agents (Ag NPs in this case). In addition, Ag NPs had a slightly lower negative surface z-potential than the MSNPs (-32.9 ± 2.8, -41.5 ± 0.3, and -38.6 ± 0.5 mV for Ag, AgCo, and AgFe NPs, respectively). Since the bacterial cell wall is negatively charged, the electrostatic repulsion of Ag NPs may be weaker than that of the MSNPs, facilitating adsorption to the cell wall and the consequent intracellular delivery of Ag^+ followed by particle internalization.

However, the concentration of Ag^+ ions released from the MSNPs was only lower by a factor of 2–4 compared to pure Ag NPs and the difference in z-potential was negligible. This suggests that a surface cooperative effect occurs in pure Ag NPs that enhances their antibacterial activity compared to MSNPs, whose surface composition also includes Fe or Co. As such, the overall antimicrobial effect may be optimized as effective bactericidal agents by using Ag NPs in synergy with AgCo or AgFe NPs, which can then be made to respond to external magnetic fields in order to disrupt the bacterial biofilm.

Biofilm deterioration

Biofilm deterioration analysis was performed using *E. faecalis*, *E. cloacae*, and *B. subtilis* as they are better able to grow homogeneous solid and reproducible biofilms than *P. putida*,[74] and they support staining by a wide variety of dyes, a necessary condition when employing Confocal Laser Scanning Microscopy (CLSM). Ag NPs, Ag NPs with AgFe NPs 1 : 1 mass, and Ag NPs with AgCo NPs 1 : 1 mass were added to multi-well plates containing bacterial biofilms at two different concentrations (the MEC for the corresponding bacteria and at a high concentration (HC) of 20 μg mL^{-1}). Besides, the NPs were tested with and without the application of an external magnetic field, used to promote magnetophoretic movement and the interaction of the MSNPs with the bacterial culture. The magnetic field was applied below the multi-well plates using a permanent NdFeB magnet (N45) under constant motion at ~0.25 cm s^{-1} for 9 min (Fig. 4A). Then, after staining with the SYBR green dye (15 min), the biofilms were analyzed by cross-sectional confocal microscopy to evaluate the damage qualitatively and quantitatively (Fig. 4B). Confocal images indicated that the pathogenic *E. faecalis* and *E. cloacae* biofilms suffered the most severe damage (shrinking and deterioration) when subjected to 20 μg mL^{-1} of Ag NPs with AgCo NPs and Ag NPs with AgFe NPs under the external magnetic field (Fig. 4C). Cross-sectional images showed the formation of channels trespassing deep into the biofilm, particularly in the *E. cloacae* biofilm. Some channels were also found in the biofilm treated with pure Ag NPs, presumably because the high Ag NP concentration was enough to mechanically interact with the EPS matrix through agglomeration and settling related to gravitational forces. Noteworthy, the width of the channels was greater for the MSNPs due to enhanced NP interaction driven by their magnetophoretic movement (Fig. 4C–E). In fact, after forming clusters, the MSNPs inflict damage to the biofilm as the magnetophoretic force scales up with the mass of magnetic particles.[12,75]

Moreover, the investigation of biofilm thickness confirmed that channel formation induced a reduction in biofilm thickness (Fig. 4F), with larger NP concentrations resulting in a thinner biofilm, denoting increased EPS matrix degradation. The reduction in biofilm thickness caused by the external magnetic field was well evident in all MSNP samples at NP concentrations of 20 μg mL^{-1} (Fig. 4C–E).

Nevertheless, channel formation does not ensure biofilm eradication by itself, as the remaining extracellular matrix could still provide nutrients to sustain bacterial growth and subsequent biofilm regeneration.[9] Subsequent overlayer images (Fig. 4D), however, showed that the MSNPs kept inflicting damage on the *E. cloacae* biofilm once the channels had been formed by following the movement of the magnet and simultaneously destroying the biofilm. Since the magnetophoretic force scales with the size of the clusters of NPs,[12,75] the larger clusters will follow the magnetic movement more efficiently and also at a higher translation speed compared to smaller clusters. However, in our experiment, the speed of magnet movement was tuned to attract a majority of NPs and to achieve a more proficient biofilm deterioration by a collective magnetophoretic effect. Under these conditions, the heavily extended deterioration of the *E. cloacae* biofilm achieved by MSNPs with Ag NPs leads to more efficient and long-term bacterial extermination compared to antibacterial agents alone, which are unable to exert a mechanical effect on the biofilm.

It is worth highlighting that the experiments were performed on biofilms whose maturity stage is not so advanced that the dispersal phase is reached. An advanced biofilm maturity stage may introduce additional challenges, such as reduced bacterial susceptibility to antimicrobial agents[76] or biofilm disassembly that may provide barriers preventing the free magnetic-powered movement of the NPs,[77] both requiring specific investigations. On the other hand, the magnetic field's intensity and the magnet movement's speed and frequency are parameters that need adjustments based on the biofilm maturity stage and 3D morphology.[13]

Bactericidal mechanism

The statistical analysis of biofilm perforation and thickness (Fig. 4E and F) confirmed that the biofilm formed by

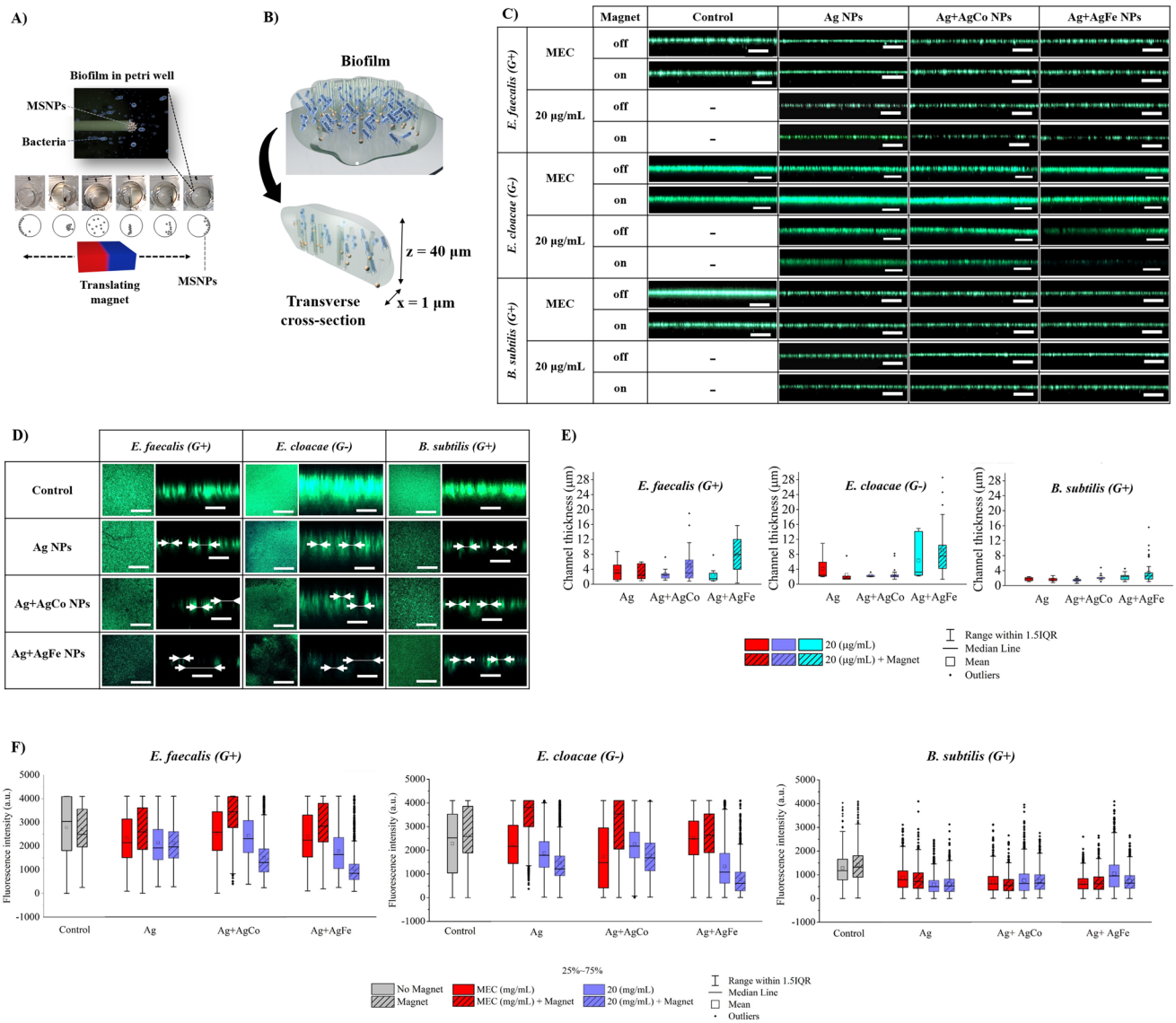

Fig. 4 (A) Artwork representing the biofilm disruption by MSNPs when following the movement of a magnet located under the petri well. As represented by the sketch circles with dots under the experiment's pictures, the MSNPs are homogeneously distributed when the magnet is centered under the petri well. However, once it is moved to the right or left, the MSNPs form clusters and follow it. As represented in the zooming sketch, the MSNPs disrupt the biofilm when the magnetic motion occurs, leading to efficient biofilm deterioration with the magnet movement. (B) Illustration of a biofilm loaded with the nanoparticles and the corresponding cross-sectional images to evaluate biofilm deterioration and perforation. (C) Representative cross-sectional biofilm images taken by CLSM in the presence (on) or absence (off) of a permanent magnetic field. Within these cross-sectional images, it is possible to appreciate the biofilm channel formation and thickness reduction produced by the MSNPs, denoting biofilm deterioration. The inset scale bars within the cross-sectional images correspond to 100 µm. (D) The overlayer or biofilm top-view (left side) image showing the macroscopically appreciable biofilm deterioration after the MSNP disruption and the zoomed image of the biofilm transversal portions (right side) showing more clearly the channels formed by the MSNPs under the influence of the magnetic field. The scale bars displayed in the biofilm overlayer images correspond to 500 µm and those in the zoomed cross-sectional images to 25 µm. Channel size was extracted from the cross-sectional images and indicated with white arrows in the corresponding zoom images (right side). (E) Box chart of channel size distribution within the biofilms after magnetically powered deterioration by NPs with a 20 µg mL^{-1} concentration. The reduced box size in *B. subtilis* is due to the low number of channels found on the inspected CLSM transversal biofilm images. (F) Relative biofilm thickness box charts before and after biofilm deterioration by the NPs at MEC and 20 µg mL^{-1} concentrations, when not applying and when applying the oscillatory magnet movement.

B. subtilis was more resistant to MSNPs than those formed by *E. faecalis* or *E. cloacae*, leading to reduced biofilm eradication. This may be a mechanical effect as this biofilm comprises non-motile cells that secrete an extracellular matrix of proteins, exopolysaccharides, motile cells, and spores, which resist MSNP movement. On the assumption that Ag NPs can trigger bacterial DNA damage *via* ROS produced through Ag^{+} interactions or the direct interaction of DNA with the surface of internalized Ag NPs, we applied the biomarker malondialdehyde (MDA) after MSNP interaction with the

biofilms to indicate membrane lipid peroxidation due to ROS action.[45] Significantly higher levels of MDA were observed in Gram-positive bacteria (*E. faecalis* and *B. subtilis*) after treating the biofilms with Ag NPs with AgFe NPs at a concentration of 20 μg mL^{-1} (Fig. 5). Moreover, MDA levels in *B. subtilis* were greater when the NPs were not exposed to the external magnetic field. In the case of the Gram-negative bacteria, *E. cloacae* responded similarly to both MSNPs, though significantly higher MDA production was observed when Ag NPs with AgCo NPs at 20 μg mL^{-1} were exposed to the magnetic field. Likewise, *P. putida* showed significantly higher MDA generation with Ag NPs and AgCo NPs at 20 μg mL^{-1} with the magnetic field. Interestingly, the magnetic field failed to trigger MDA production when MSNPs were absent, suggesting that biofilm–MSNP interaction is necessary to provoke an increase in MDA, and thus ROS generation.

MDA selective production can be understood in terms of the synergy between NP interactions with the different types of bacteria and the mechanism utilized for disrupting the biofilms. For example, the ROS produced by Ag^{+} and Co^{2+} found in AgCo and Fe^{2+} and Fe^{3+} in AgFe can undergo Fenton reactions when in contact with water, resulting in the formation of $OH^{\bullet}$ and $HO_2^{\bullet}$ radicals responsible for oxidative stress,[78] thereby increasing MDA formation.[79] Thus, even when the amount of Ag^{+} released is lower for Ag + AgCo and Ag + AgFe, the ROS produced by the doping elements can still accumulate with those from Ag, ensuring increased MDA production with NP concentrations of 20 μg mL^{-1}. On the other hand, the magnetically powered movement of the MSNPs through the biofilm allows for their interaction with increasing numbers of bacteria, again resulting in increased MDA production (apart from *B. subtilis*, owing to its resistance to MNP magnetophoretic movement). It has been demonstrated that the *B. subtilis* biofilm can absorb certain metal ions, including Fe^{2+} and Fe^{3+}, into the biofilm matrix, thereby becoming more resilient to erosion by shear forces.[80] Moreover, it is worth highlighting that, as for any other gammaproteobacteria, Co is an obligate nutrient for *E. cloacae* and *P. putida*.[81,82] Thus, Co doping provides magnetophoretic motility to the Ag NPs and enhances their interaction with both types of bacteria through their potential absorption due to their Co content. However, as the AgCo NPs are mainly composed of Ag, even when the said absorption could be minimal, this process can lead to the proximity of the Ag content towards the bacteria resulting in an increase in ROS and, with this, MDA production. Finally, for Ag NPs, it is known that ROS generation and subsequent MDA production are principally mediated by the interaction between the ions released and the bacterial membrane.[83] Since the Ag NPs cannot move in the biofilm under the external magnetic field, their interaction is restricted to the superficial region of the biofilm, where the NPs settle by gravity, reducing MDA production.

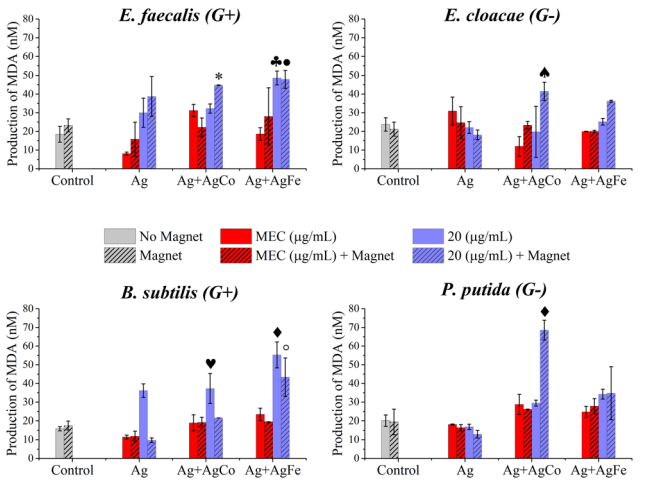

Fig. 5 Amount of MDA detected after biofilm deterioration by NPs at MEC and 20 μg mL^{-1} concentrations, both with and without the application of an oscillatory magnetic field. The controls consisted of biofilms with no NPs, with and without the application of the magnetic field. Data were expressed as the mean value (± standard deviation). Significance levels were *P = 0.0186, ♣P = 0.0064, ●P = 0.0078, ♠P = 0.0253, ♥P = 0.0032, ○P = 0.0002, and ◆P < 0.0001 *vs.* the corresponding control.

Cell cytotoxicity

Cell cytotoxicity studies are important to gather information in response to the increasing concerns about the possible impact of Ag-based antimicrobials on the environment, when they are cleared from patients or released from substrates and products.[30,31] In our case, these data are particularly interesting because the doping of Ag with transition elements like Fe or Co may alter the biocompatibility of NPs. In particular, in the case of Co, where higher cytotoxicity was observed upon the release of AgCo core–shell NPs from antibacterial polymeric matrixes,[16] and Co is considered an environmental pollutant if it exceeds the trace limits (10 mg L^{-1}).[84,85] The cytotoxicity experiments were performed on human cells (T47D—breast carcinoma) and rainbow trout cells (RT— gills) as examples of mammalian and fish fauna exposed to the NPs.

In both the cell lines, the Ag NPs doped with the magnetic elements are associated with lower cytotoxicity than pure Ag NPs (Fig. 6). It is worth noting that Ag NP cytotoxicity is related to particle size, but in this case, the NPs have similar size distribution,[23,62,65] suggesting that size is not the origin of the observed difference of cytotoxicity. Instead, the results are in agreement with the lower Ag ion release measured for the AgCo and AgFe NPs. Overall, the T47D cell line well tolerated the doped Ag NPs, even at 40–60 mg L^{-1}. Instead, the RT cell line was especially susceptible to the Ag content, as previously observed in similar experiments of exposure to Ag^{+} ions.[86] In general, these results further confirm the benefits of combining Ag NPs with MSNPs to efficiently disrupt biofilms at lower concentrations of Ag but also highlight the need for the careful exploitation of the Ag NPs to avoid environmental risks, for instance, for fish fauna which is very sensitive to Ag ions.

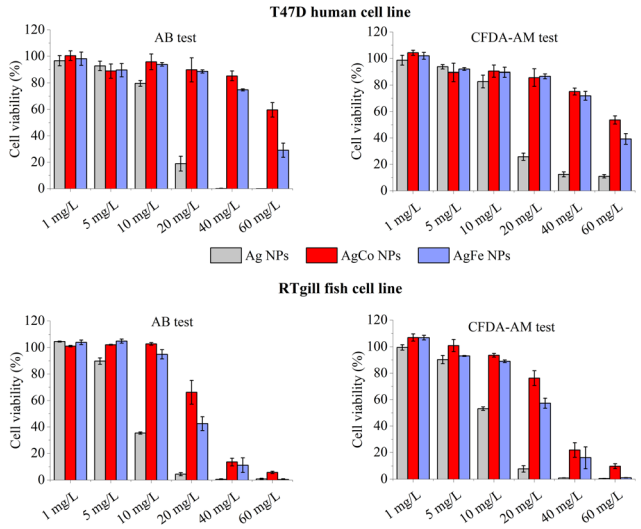

Fig. 6 Cell viability of T47D (breast carcinoma human cells) and RT (gills fish cells) evaluated through cellular metabolic activity (AB) and cell membrane integrity (CFDA-AM). The cells were incubated for 24 h with Ag, AgCo or AgFe NPs.

Conclusions

In summary, we showed that Ag NPs doped with magnetic elements such as Fe or Co can synergize with pure Ag NPs to increase antimicrobial efficacy by deteriorating bacterial biofilms under an external magnetic field. This is achieved by the simultaneous production of ROS, primarily due to the release of Ag^+ ions in coaction with mechanical damage and permeation of the bacterial biofilm through the magnetophoretic movement of the doped magnetic MSNPs, with those doped with Fe exerting the most biofilm damage. This synergy paves the way for more effective delivery of Ag^+ throughout the biofilm. Antibacterial agents with a magnetic responsive component are likely to be more efficient for treating biofilms normally difficult to eradicate, such as those produced by *E. faecalis* or *E. cloacae*, which represent a primary threat in the health sector by causing hospital-acquired infections.[87,88] In addition, selective MDA generation in Gram-negative bacteria indicates that selecting appropriate bacterial nutrients to dope Ag NPs (such as Co or Fe) can result in improved ROS generation and, subsequently, bacterial eradication, which is of particular interest for the extermination of bacteria that can serve as exchange platforms for ARGs like *P. putida*.[72]

The increase in the efficacy of Ag antibacterial agents as well as the expansion of their action to biofilm deterioration are key steps towards the reduction of Ag NP dosage, resulting in the improvement of the risk/benefits ratio. This is required to limit the selection of Ag-resistant bacteria and to avoid the alteration of the microbial communities in the natural ecosystem receiving Ag NP waste.[31] Regarding these relevant issues, we believe that the methods outlined in this study show additional positive prospects, particularly in tailoring doped MSNPs using LAL, an environmentally friendly method. A key feature of LAL is that NPs are obtained free of ligands or organic contaminants, meaning they can be tested pure or following surface conjugation with specific ligands. The conjugation of such MSNPs with other suitable antibacterial or biofilm penetrating agents will open many new possibilities in bacterial control and the realization of a safer living environment.

Author contributions

Rafael Torres-Mendieta: conceptualization, data curation, formal analysis, investigation, methodology, project administration, resources, software, supervision, validation, visualization, writing – original draft, and writing – review & editing. Nhung H. A. Nguyen: data curation, formal analysis, investigation, methodology, and writing – review & editing. Andrea Guadagnini: investigation and methodology. Jaroslav Semerad: investigation, methodology, resources, software, and writing – review & editing. Dariusz Łukowiec: resources, software, and writing – review & editing. Petr Parma: formal analysis, methodology, resources, software, and validation. Jijin Yang: formal analysis, methodology, resources, software, and validation. Stefano Agnoli: formal analysis, methodology, resources, software, validation, and writing – review & editing. Alena Sevcu: resources, software, validation, and writing – review & editing. Tomas Cajthaml: resources, software, validation, and writing – review & editing. Miroslav Cernik: funding acquisition, resources, software, validation, and writing – review & editing. Vincenzo Amendola: conceptualization, data curation, formal analysis, funding acquisition, investigation, methodology, project administration, resources, software, supervision, validation, visualization, writing – original draft, and writing – review & editing.

Conflicts of interest

There are no conflicts to declare.

Acknowledgements

The research presented in this article was supported by the Ministry of Education, Youth and Sports of the Czech Republic through the Research Infrastructures NanoEnviCz (Project No. LM2018124) and through the European Structural and Investment Funds under the framework of the Operational Programme – Research, Development and Education project entitled Hybrid Materials for Hierarchical Structures (HyHi, Reg. no. CZ.02.1.01/0.0/0.0/16_019/0000843). In addition, we gratefully acknowledge the permission to use the Microscopy Facility of the Institute of Microbiology, Czech Academy of Sciences, Vídenská 1083, Prague, CZ and the support provided by the staff. The authors, in addition, would like to thank Tereza Müllerová for the assistance with the *in vitro* cytotoxicity experiments. DŁ is grateful for the support from the

International Visegrad Fund (Visegrad Scholarship, Grant ID: 52210829). V. A. thanks Vito Coviello and Michael Bissoli for their help with NP synthesis and acknowledges funding from the University of Padova STARS grant "4NANOMED" and the P-DiSC project "DYNAMO".

References

1 E. Bakkeren, M. Diard and W. D. Hardt, *Nat. Rev. Microbiol.*, 2020, **18**, 479–490, DOI: **10.1038/s41579-020-0378-z**.
2 H. C. Flemming, J. Wingender, U. Szewzyk, P. Steinberg, S. A. Rice and S. Kjelleberg, *Nat. Rev. Microbiol.*, 2016, **14**, 563–575, DOI: **10.1038/nrmicro.2016.94**.
3 J. W. Costerton, P. S. Stewart and E. P. Greenberg, *Science*, 1999, **284**, 1318–1322.
4 E. Z. Ron and E. Rosenberg, *Environ. Microbiol.*, 2001, **3**, 229–236, DOI: **10.1046/j.1462-2920.2001.00190.x**.
5 Ł. Ławniczak, M. Woźniak-Karczewska, A. P. Loibner, H. J. Heipieper and Ł. Chrzanowski, *Molecules*, 2020, **25**, 856, DOI: **10.3390/molecules25040856**.
6 J. G. Leid and M. Shirtliff, *The Role of Biofilms in Device-Related Infections*, 2009, DOI: **10.1007/978-3-540-68119-9**.
7 J. W. Costerton, K. J. Cheng, G. G. Geesey, T. I. Ladd, J. C. Nickel, M. Dasgupta and T. J. Marrie, *Annu. Rev. Microbiol.*, 1987, **41**, 435–464, DOI: **10.1146/annurev.mi.41.100187.002251**.
8 H. P. de Vladar, M. Santos and E. Szathmáry, *Trends Ecol. Evol.*, 2017, **32**, 324–334, DOI: **10.1016/j.tree.2017.01.008**.
9 H. Koo, R. N. Allan, R. P. Howlin, P. Stoodley and L. Hall-Stoodley, *Nat. Rev. Microbiol.*, 2017, **15**, 740–755, DOI: **10.1038/nrmicro.2017.99**.
10 M. Boholm and R. Arvidsson, *J. Cleaner Prod.*, 2014, **68**, 135–143, DOI: **10.1016/j.jclepro.2013.12.058**.
11 F. Robertson, S. C. Jagers and B. Rönnerstrand, *Sustainability*, 2018, **10**, 143, DOI: **10.3390/su10010143**.
12 Z. Jin, K. T. Nguyen, G. Go, B. Kang, H. K. Min, S. J. Kim, Y. Kim, H. Li, C. S. Kim, S. Lee, S. Park, K. P. Kim, K. M. Huh, J. Song, J. O. Park and E. Choi, *Nano Lett.*, 2019, **19**, 8550–8564, DOI: **10.1021/acs.nanolett.9b03051**.
13 K. Quan, Z. Zhang, H. Chen, X. Ren, Y. Ren, B. W. Peterson, H. C. van der Mei and H. J. Busscher, *Small*, 2019, **15**, 1902313, DOI: **10.1002/smll.201902313**.
14 S. Cheeseman, A. J. Christofferson, R. Kariuki, D. Cozzolino, T. Daeneke, R. J. Crawford, V. K. Truong, J. Chapman and A. Elbourne, *Adv. Sci.*, 2020, **7**, 1902913, DOI: **10.1002/advs.201902913**.
15 Z. Kanwal, M. A. Raza, S. Riaz, S. Manzoor, A. Tayyeb, I. Sajid and S. Naseem, *R. Soc. Open Sci.*, 2019, **6**, 182135, DOI: **10.1098/rsos.182135**.
16 A. Alonso, X. Muñoz-Berbel, N. Vigués, R. Rodríguez-Rodríguez, J. MacAnás, M. Muñoz, J. Mas and D. N. Muraviev, *Adv. Funct. Mater.*, 2012, **23**, 2450–2458, DOI: **10.1002/adfm.201202663**.
17 G. Hwang, A. J. Paula, E. E. Hunter, Y. Liu, A. Babeer, B. Karabucak, K. Stebe, V. Kumar, E. Steager and H. Koo, *Sci. Rob.*, 2019, **4**, eaaw2388, DOI: **10.1126/scirobotics.aaw2388**.
18 R. Di Corato, D. Palumberi, R. Marotta, M. Scotto, S. Carregal-Romero, P. Rivera-Gil, W. J. Parak and T. Pellegrino, *Small*, 2012, **8**, 2731–2742, DOI: **10.1002/smll.201200230**.
19 L. Eberson, *Adv. Phys. Org. Chem.*, 1982, **18**, 79–185, DOI: **10.1016/S0065-3160(08)60139-2**.
20 J. W. McLeod and J. Gordon, *Biochem. J.*, 1922, **16**, 499–506, DOI: **10.1042/bj016049**.
21 L. Gao, Y. Liu, D. Kim, Y. Li, G. Hwang, P. C. Naha, D. P. Cormode and H. Koo, *Biomaterials*, 2016, **101**, 272–284, DOI: **10.1016/j.biomaterials.2016.05.051**.
22 M. Mahmoudi, S. Sant, B. Wang, S. Laurent and T. Sen, *Adv. Drug Delivery Rev.*, 2011, **63**, 24–46, DOI: **10.1016/j.addr.2010.05.006**.
23 P. Makvandi, C. Y. Wang, E. N. Zare, A. Borzacchiello, L. N. Niu and F. R. Tay, *Adv. Funct. Mater.*, 2020, **30**, 1910021, DOI: **10.1002/adfm.201910021**.
24 E. Sánchez-López, D. Gomes, G. Esteruelas, L. Bonilla, A. L. Lopez-Machado, R. Galindo, A. Cano, M. Espina, M. Ettcheto, A. Camins, A. M. Silva, A. Durazzo, A. Santini, M. L. Garcia and E. B. Souto, *Nanomaterials*, 2020, **10**, 292, DOI: **10.3390/nano10020292**.
25 S. Agnihotri, S. Mukherji and S. Mukherji, *Nanoscale*, 2013, **5**, 7328–7340, DOI: **10.1039/c3nr00024a**.
26 X. Wang, J. Wu, P. Li, L. Wang, J. Zhou, G. Zhang, X. Li, B. Hu and X. Xing, *ACS Appl. Mater. Interfaces*, 2018, **10**, 34905–34915, DOI: **10.1021/acsami.8b10972**.
27 V. Vedarethinam, L. Huang, W. Xu, R. Zhang, D. D. Gurav, X. Sun, J. Yang, R. Chen and K. Qian, *Small*, 2019, **15**, 1803051, DOI: **10.1002/smll.201803051**.
28 Y. Luengo, B. Sot and G. Salas, *Colloids Surf., B*, 2020, **194**, 111178, DOI: **10.1016/j.colsurfb.2020.111178**.
29 A. L. Padilla-Cruz, J. A. Garza-Cervantes, X. G. Vasto-Anzaldo, G. García-Rivas, A. León-Buitimea and J. R. Morones-Ramírez, *Sci. Rep.*, 2021, **11**, 5351, DOI: **10.1038/s41598-021-84768-8**.
30 O. McNeilly, R. Mann, M. Hamidian and C. Gunawan, *Front. Microbiol.*, 2021, **12**, 652863, DOI: **10.3389/fmicb.2021.652863**.
31 K. Yonathan, R. Mann, K. R. Mahbub and C. Gunawan, *Environ. Pollut.*, 2022, **293**, 118506, DOI: **10.1016/j.envpol.2021.118506**.
32 R. Mann, A. Holmes, O. McNeilly, R. Cavaliere, G. A. Sotiriou, S. A. Rice and C. Gunawan, *J. Nanobiotechnol.*, 2021, **19**, 1–17, DOI: **10.1186/s12951-021-01027-8**.
33 E. Valentin, A. L. Bottomley, G. S. Chilambi, E. J. Harry, R. Amal, G. A. Sotiriou, S. A. Rice and C. Gunawan, *Nanoscale*, 2020, **12**, 2384–2392, DOI: **10.1039/c9nr08424j**.
34 V. Amendola, D. Amans, Y. Ishikawa, N. Koshizaki, S. Scirè, G. Compagnini, S. Reichenberger and S. Barcikowski, *Chem. – Eur. J.*, 2020, **26**, 9206–9242, DOI: **10.1002/chem.202000686**.

35 S. Scaramuzza, S. Polizzi and V. Amendola, *Nanoscale Adv.*, 2019, **1**, 2681–2689, DOI: **10.1039/c9na00143c**.
36 A. Guadagnini, S. Agnoli, D. Badocco, P. Pastore, D. Coral, M. B. Fernàndez van Raap, D. Forrer and V. Amendola, *J. Colloid Interface Sci.*, 2021, **585**, 267–275, DOI: **10.1016/j.jcis.2020.11.089**.
37 D. Ettel, O. Havelka, S. Isik, D. Silvestri, S. Wacławek, M. Urbánek, V. V. T. Padil, M. Černík, F. Yalcinkaya and R. Torres-Mendieta, *Appl. Surf. Sci.*, 2021, **564**, 150471, DOI: **10.1016/J.APSUSC.2021.150471**.
38 A. Barchanski, *Laser-generated functional nanoparticle bioconjugates: Design for application in biomedical science and reproductive biology*, Springer Spektrum, Berlin, Germany, 2016, DOI: **10.1007/978-3-658-13515-7**.
39 V. Amendola, S. Scaramuzza, S. Agnoli, G. Granozzi, M. Meneghetti, G. Campo, V. Bonanni, F. Pineider, C. Sangregorio, P. Ghigna, S. Polizzi, P. Riello, S. Fiameni and L. Nodari, *Nano Res.*, 2015, **8**, 4007–4023, DOI: **10.1007/s12274-015-0903-y**.
40 W. T. Nichols, T. Sasaki and N. Koshizaki, *J. Appl. Phys.*, 2006, **100**, 114911, DOI: **10.1063/1.2390640**.
41 D. M. Mitrano, J. F. Ranville, A. Bednar, K. Kazor, A. S. Hering and C. P. Higgins, *Environ. Sci. Nano*, 2014, **1**, 248–259, DOI: **10.1039/c3en00108c**.
42 J. Vidmar, K. Loeschner, M. Correia, E. H. Larsen, P. Manser, A. Wichser, K. Boodhia, Z. S. Al-Ahmady, J. Ruiz, D. Astruc and T. Buerki-Thurnherr, *Nanoscale*, 2018, **10**, 11980–11991, DOI: **10.1039/c8nr02096e**.
43 A. Rua-Ibarz, E. Bolea-Fernandez, G. Pozo, X. Dominguez-Benetton, F. Vanhaecke and K. Tirez, *J. Anal. At. Spectrom.*, 2020, **35**, 2023–2032, DOI: **10.1039/d0ja00183j**.
44 S. Suppi, K. Kasemets, A. Ivask, K. Künnis-Beres, M. Sihtmäe, I. Kurvet, V. Aruoja and A. Kahru, *J. Hazard. Mater.*, 2015, **286**, 75–84, DOI: **10.1016/j.jhazmat.2014.12.027**.
45 J. Semerád, M. Čvančarová, J. Filip, J. Kašlík, J. Zlotá, J. Soukupová and T. Cajthaml, *Chemosphere*, 2018, **213**, 568–577, DOI: **10.1016/j.chemosphere.2018.09.029**.
46 K. Michalíková, L. Linhartová, M. Ezechiáš and T. Cajthaml, *Chemosphere*, 2019, **217**, 534–541, DOI: **10.1016/j.chemosphere.2018.11.006**.
47 K. Šrédlová, S. Šilhavecká, L. Linhartová, J. Semerád, K. Michalíková, M. Pivokonský and T. Cajthaml, *Toxicon*, 2021, **195**, 69–77, DOI: **10.1016/j.toxicon.2021.03.003**.
48 W. Hume-Rothery, *London, Edinburgh Dublin Philos. Mag. J. Sci.*, 1936, **22**, 1013–1047, DOI: **10.1080/14786443608561755**.
49 I. Karakaya and W. T. Thompson, *Bull. Alloy Phase Diagrams*, 1986, **7**, 259–263, DOI: **10.1007/BF02869002**.
50 L. J. Swartzendruber, *Bull. Alloy Phase Diagrams*, 1984, **5**, 560–564, DOI: **10.1007/BF02868316**.
51 V. Amendola, S. Scaramuzza, L. Litti, M. Meneghetti, G. Zuccolotto, A. Rosato, E. Nicolato, P. Marzola, G. Fracasso, C. Anselmi, M. Pinto and M. Colombatti, *Small*, 2014, **10**, 2476–2486, DOI: **10.1002/smll.201303372**.
52 T. Tsuji, T. Hamagami, T. Kawamura, J. Yamaki and M. Tsuji, *Appl. Surf. Sci.*, 2005, **243**, 214–219, DOI: **10.1016/j.apsusc.2004.09.065**.
53 P. Andreazza, A. Lemoine, A. Coati, D. Nelli, R. Ferrando, Y. Garreau, J. Creuze and C. Andreazza-Vignolle, *Nanoscale*, 2021, **13**, 6096–6104, DOI: **10.1039/d0nr08862e**.
54 V. Amendola, V. Torresan, D. Forrer, A. Guadagnini, D. Badocco, P. Pastore, M. Casarin, A. Selloni, D. Coral, M. Ceolin, M. B. Fernàndez van Raap, A. Busato, P. Marzola and A. E. Spinelli, *ACS Nano*, 2020, **14**, 12840–12853, DOI: **10.1021/acsnano.0c03614**.
55 S. Scaramuzza, S. Agnoli and V. Amendola, *Phys. Chem. Chem. Phys.*, 2015, **17**, 28076–28087, DOI: **10.1039/c5cp00279f**.
56 K. P. Miller, L. Wang, B. C. Benicewicz and A. W. Decho, *Chem. Soc. Rev.*, 2015, **44**, 7787–7807, DOI: **10.1039/C5CS00041F**.
57 C. Y. Shih, R. Streubel, J. Heberle, A. Letzel, M. V. Shugaev, C. Wu, M. Schmidt, B. Gökce, S. Barcikowski and L. V. Zhigilei, *Nanoscale*, 2019, **10**, 035001, DOI: **10.1088/2043-6254/ab2e6e**.
58 R. Baiee, Z. Liu and L. Li, *Adv. Nat. Sci.: Nanosci. Nanotechnol.*, 2018, **10**, 6900–6910, DOI: **10.1039/c7nr08614h**.
59 A. M. Ferraria, A. P. Carapeto and A. M. Botelho do Rego, *Vacuum*, 2012, **86**, 1988–1991, DOI: **10.1016/j.vacuum.2012.05.031**.
60 A. Van der Meeren, K. Devilliers, S. Coudert, A. Moureau, M. Defrance, C. Berthomieu and V. Malard, *Toxicol. In Vitro*, 2022, **84**, 105448, DOI: **10.1016/j.tiv.2022.105448**.
61 O. K. Borggaard, *J. Soil Sci.*, 1976, **27**, 478–486, DOI: **10.1111/j.1365-2389.1976.tb02017.x**.
62 N. Durán, M. Durán, M. B. de Jesus, A. B. Seabra, W. J. Fávaro and G. Nakazato, Nanomedicine Nanotechnology, *Biol. Med.*, 2016, **12**, 789–799, DOI: **10.1016/j.nano.2015.11.016**.
63 H. Li, J. Chen, H. Fan, R. Cai, X. Gao, D. Meng, Y. Ji, C. Chen, L. Wang and X. Wu, *Nanoscale*, 2020, **12**, 6429–6437, DOI: **10.1039/c9nr08621h**.
64 B. Le Ouay and F. Stellacci, *Nano Today*, 2015, **10**, 339–354, DOI: **10.1016/j.nantod.2015.04.002**.
65 C. Marambio-Jones and E. M. V. Hoek, *J. Nanopart. Res.*, 2010, **12**, 1531–1551, DOI: **10.1007/s11051-010-9900-y**.
66 G. Huang, H. Chen, Y. Dong, X. Luo, H. Yu, Z. Moore, E. A. Bey, D. A. Boothman and J. Gao, *Theranostics*, 2013, **3**, 116–126, DOI: **10.7150/thno.5411**.
67 L. O. Simonsen, H. Harbak and P. Bennekou, *Sci. Total Environ.*, 2012, **432**, 210–215, DOI: **10.1016/j.scitotenv.2012.06.009**.
68 G. C. F. Clark and D. F. Williams, *J. Biomed. Mater. Res.*, 1982, **16**, 125–134, DOI: **10.1002/jbm.820160205**.
69 R. Rashid, A. Cazenave-Gassiot, I. H. Gao, Z. J. Nair, J. K. Kumar, L. Gao, K. A. Kline and M. R. Wenk, *PLoS One*, 2017, **12**, e0175886, DOI: **10.1371/journal.pone.0175886**.
70 F. Liu, F. Wang, L. Du, T. Zhao, M. P. Doyle, D. Wang, X. Zhang, Z. Sun and W. Xu, *Food Control*, 2018, **84**, 442–448, DOI: **10.1016/j.foodcont.2017.09.004**.
71 X. Z. Li and H. Nikaido, *Drugs*, 2009, **69**, 1555–1623, DOI: **10.2165/11317030-000000000-00000**.

72 S. Peter, P. Oberhettinger, L. Schuele, A. Dinkelacker, W. Vogel, D. Dörfel, D. Bezdan, S. Ossowski, M. Marschal, J. Liese and M. Willmann, *BMC Genomics*, 2017, **18**, 859, DOI: 10.1186/s12864-017-4216-2.

73 E. B. Gajan, A. Shirmohammadi, M. Aghazadeh, M. Alizadeh, A. S. Deljavan and F. Ahmadpour, *J. Dent. Res. Dent. Clin. Dent. Prospects*, 2013, **7**, 102–104, DOI: 10.5681/joddd.2013.018.

74 V. Wigneswaran, K. F. Nielsen, C. Sternberg, P. R. Jensen, A. Folkesson and L. Jelsbak, *Microb. Cell Fact.*, 2016, **15**, 181, DOI: 10.1186/s12934-016-0581-9.

75 H. Gavilán, K. Simeonidis, E. Myrovali, E. Mazarío, O. Chubykalo-Fesenko, R. Chantrell, L. Balcells, M. Angelakeris, M. P. Morales and D. Serantes, *Nanoscale*, 2021, **13**, 15631–15646, DOI: 10.1039/d1nr03484g.

76 P. Thuptimdang, T. Limpiyakorn, J. McEvoy, B. M. Prüß and E. Khan, *J. Hazard. Mater.*, 2015, **290**, 127–133, DOI: 10.1016/j.jhazmat.2015.02.073.

77 H. Vlamakis, Y. Chai, P. Beauregard, R. Losick and R. Kolter, *Nat. Rev. Microbiol.*, 2013, **11**, 157–168, DOI: 10.1038/nrmicro2960.

78 M. Valko, C. J. Rhodes, J. Moncol, M. Izakovic and M. Mazur, *Chem.-Biol. Interact.*, 2006, **160**, 1–40, DOI: 10.1016/j.cbi.2005.12.009.

79 J. Semerad, N. I. N. Pacheco, A. Grasserova, P. Prochazkova, M. Pivokonsky, L. Pivokonska and T. Cajthaml, *Nanomaterials*, 2020, **10**, 2189, DOI: 10.3390/nano10112189.

80 S. Grumbein, M. Opitz and O. Lieleg, *Metallomics*, 2014, **6**, 1441–1450, DOI: 10.1039/c4mt00049h.

81 S. Ghosh, J. Bhattacharya, R. Nitnavare and T. J. Webster, in *Development in Wastewater Treatment Research and Processes: Microbial Degradation of Xenobiotics through Bacterial and Fungal Approach*, ed. S. R.-C. Maulin and P. Shah, Elsevier, 2022, pp. 131–158. DOI: 10.1016/B978-0-323-85839-7.00011-6.

82 P. Ray, V. Girard, M. Gault, C. Job, M. Bonneu, M. A. Mandrand-Berthelot, S. S. Singh, D. Job and A. Rodrigue, *Metallomics*, 2013, **5**, 68–79, DOI: 10.1039/c2mt20147j.

83 A. Onodera, F. Nishiumi, K. Kakiguchi, A. Tanaka, N. Tanabe, A. Honma, K. Yayama, Y. Yoshioka, K. Nakahira, S. Yonemura, I. Yanagihara, Y. Tsutsumi and Y. Kawai, *Toxicol. Rep.*, 2015, **2**, 574–579, DOI: 10.1016/j.toxrep.2015.03.004.

84 P. C. Nagajyoti, K. D. Lee and S. Tvm, *Environ. Chem. Lett.*, 2010, **8**, 199–216, DOI: 10.1007/s10311-010-0297-8.

85 L. Tofan, *Polymers*, 2022, **14**, 1647, DOI: 10.3390/polym14091647.

86 M. Connolly, M. L. Fernandez-Cruz, A. Quesada-Garcia, L. Alte, H. Segner and J. M. Navas, *Int. J. Environ. Res. Public Health*, 2015, **12**, 5386–5405, DOI: 10.3390/ijerph120505386.

87 J. H. Ch'ng, K. K. L. Chong, L. N. Lam, J. J. Wong and K. A. Kline, *Nat. Rev. Microbiol.*, 2019, **17**, 82–94, DOI: 10.1038/s41579-018-0107-z.

88 A. Davin-Regli and J. M. Pagès, *Front. Microbiol.*, 2015, **6**, 392, DOI: 10.3389/fmicb.2015.00392.